JMEPEG (2021) 30:7989–7997
https://doi.org/10.1007/s11665-021-06000-y

1059-9495/$19.00

Effect of Heat Input on Microstructure and Mechanical Properties of Friction Stir Welded AA2024 and AA7075 Dissimilar Alloys

Shun Xiao, Yongfang Deng, Jincheng Zeng, Weichao Zhang, and Lirong Huang

Submitted: 6 January 2021 / Revised: 3 June 2021 / Accepted: 7 June 2021 / Published online: 8 July 2021

In this study, the heat input from friction stir welding of AA2024 and AA7075 dissimilar alloys was calculated, and the relationship between the heat input and mechanical properties was studied in detail. Additionally, the effect of heat on welding was analyzed. When the welding parameters were 800 rpm-400 mm/min, the Ultimate tensile strength of the joint was at its highest (346 MPa), and the elongation was 3%. A significantly higher or lower temperature led to lower tensile strength and elongation. Too low heat input failed to deform the material completely, and the fluidity of the material formed from the two base metals was poor. Excessive heat input led to the dissolution of precipitates, grain coarsening, reduced grain bonding, and other microstructural changes. When the heat input is higher, the cooling rate is faster, which can easily cause holes at the bonding interface. In the stir zone, owing to the difference in the thermal gradient of the upper and lower parts, the bottom of the material is not softened completely owing to the lack of heat, and stress concentration occurs.

Keywords AA2024 aluminum alloy, AA7075 aluminum alloy, dissimilar alloys, FSW, heat input

1. Introduction

Aluminum alloy AA2024 has a high strength-to-weight ratio, and is mainly used for manufacturing aircraft skeleton parts, skins, and other high-load parts (Ref 1). AA7075 has a high specific strength and good weldability; moreover, it is widely used in the upper skin of aircraft wings, in fuselage frames and ribs, and in ship structures, and high-speed trains (Ref 2). In practical applications and production, different materials are selected for various parts according to the performance requirements of the actual working conditions, manufacturing process, and cost, and the welding of 2024 and 7075 aluminum alloys is inevitable. Conventional fusion welding of aluminum and its alloys results in defects (porosity and hot cracking) in the fusion zone, which significantly affect the mechanical properties of the joints (Ref 3, 4). Therefore, it is necessary to adopt novel methods to reduce or eliminate these problems.

Friction stir welding (FSW) is a solid-state welding technique invented in 1991 at The Welding Institute (TWI), UK (Ref 5). Owing to the low heat input during welding, FSW can effectively avoid hot cracking, porosity, and other defects caused by fusion welding (Ref 6, 7). Additionally, the tensile strength of FSW-welded specimens is greater than that of fusion-welded joints (Ref 8). FSW is a promising welding technique for joining lightweight alloys, and is widely used in the welding of aluminum alloys (Ref 9). Although FSW of metals and alloys is relatively easy to implement, using different welding parameters to weld dissimilar materials changes the microstructure, affecting the mechanical properties of the joint. Therefore, it is crucial to understand the microstructure development in FSW and how it affects the mechanical properties of the joint.

Owing to the large temperature gradients and plastic flow of FSW, the microstructure of the welded joint changes. Generally, the microstructure of a joint can be divided into four areas: stir zone (SZ), thermo-mechanical affected zone (TMAZ), heat-affected zone (HAZ), and base metal (BM) (Ref 10). Various studies have focused on FSW joints. Radisavljevic et al. (Ref 11) studied FSW of AA2024, and established that the particles in the SZ were the finest. Studies have shown that the weakest regions of FSW joints of 7075 alloy are generally in the TMAZ and HAZ, where the hardness values are low (Ref 12, 13). This is mainly because of the high weld heat input in these areas, leading to the coarsening of the precipitates and grains. Some precipitates can be dissolved in the SZ of 7075-T6 after FSW. This indicates that the welding temperature is higher than the solution temperature of the hardening precipitate, but lower than the melting temperature of the alloy, which is between 450 and 480 °C (Ref 14). Zhang et al. (Ref 15) established that, owing to the thermal cycle generated in AA2024 / AA7075 FSW, the precipitates in the TMAZ were coarsened, and the grains in the TMAZ were more twisted and bent than those in the BM. Research on the FSW of 2024 and 6061 aluminum alloys established that the materials in the dynamic recrystallization (DRX) region were exposed to a lower temperature than materials in the SZ far away from the TMAZ. The grain size in the SZ adjacent to the TMAZ (DRX region) is finer than that in areas far away from the TMAZ (DRX and continuous grain growth region). In contrast, the lower temperature of the

Shun Xiao and **Lirong Huang**, Mechanical and Electrical Engineering, Jiangxi University of Science and Technology, Ganzhou 341000, China; and **Yongfang Deng, Jincheng Zeng,** and **Weichao Zhang**, Engineering Research Institute, Jiangxi University of Science and Technology, Ganzhou 341000, China. Contact e-mails: dengyongfang@jxust.edu.cn and huanglirong@sina.com.

DRX region results in smaller $CuAl_2$ precipitates (Ref 16). The high temperature and plastic deformation in the SZ will lead to the refinement of crystal grains and dissolution or re-precipitation of the precipitated phase (Ref 17). Extensive precipitates are re-precipitated in the SZ at a high heat input (Ref 18).

In summary, the microstructure of the FSW affects the mechanical properties of the joint, and the heat input is crucial to the microstructural changes of the joint. Although the different microstructures of FSW joints have been studied to a certain extent, the effect of heat input on the microstructures of FSW joints of AA2024 and AA7075 dissimilar alloys is unclear. Therefore, this study evaluates the microstructural characteristics of AA2024/AA7075 dissimilar aluminum alloy FSW. Additionally, the precipitate distributions of the welded joints were analyzed through scanning electron microscopy (SEM), energy dispersive spectroscopy (EDS), and x-ray diffraction (XRD), and these observations were then related to the mechanical properties of the welds.

Table 1 Chemical composition (Wt%)

Materials	Cu	Mg	Mn	Fe	Si	Zn	Al
AA2024-T3	4.5	1.3	0.56	0.23	0.09	0.08	Bal
AA7075-T6	1.59	1.61	0.30	0.50	0.27	5.7	Bal

Table 2 Mechanical properties

Alloy	Yield strength, MPa	Ultimate tensile strength, MPa	Microhardness, HV
AA2024-T3	360	465	141
AA7075-T6	455	505	158

2. Experimental Procedure

In this study, the base materials were AA2024-T3 and AA7075-T6 aluminum alloys. The dimensions of the welded plates were 200 × 100 × 3.2 mm. The chemical compositions of the alloys are listed in Table 1. The mechanical properties are listed in Table 2.

A rotary tool, with a 14 mm diameter concave shoulder and a 2.7 mm long tapered thread pin, was used. The top diameter of the pin was 3 mm, and the inclination angle was 14° (see Fig. 1a). A gantry numerical control FSW machine was used for welding, as shown in Fig. 1(b). Prior to welding, dirt and oxide layers were removed from the plates. The plates were rigidly clamped. Welding was performed at various rotational

Table 3 Welding parameters

Process parameters	Tool rotation speed (rpm)	Feed rate (mm/min)
Specimen 1	600	400
Specimen 2	600	300
Specimen 3	800	400
Specimen 4	800	300
Specimen 5	1000	400
Specimen 6	1000	300

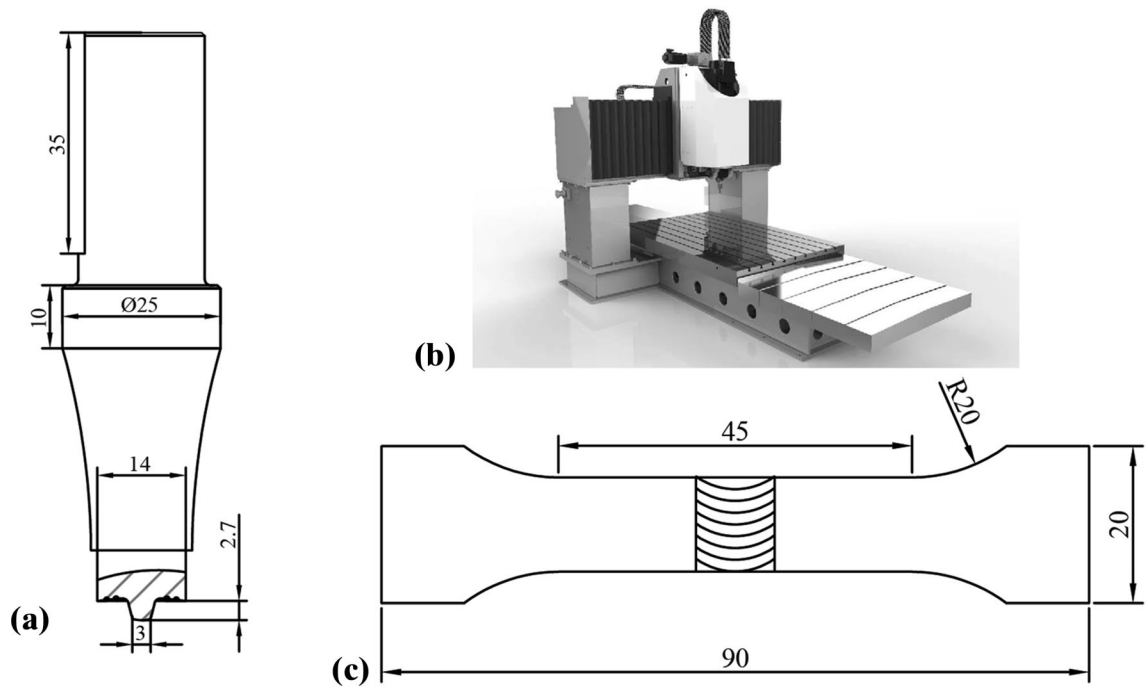

Fig. 1 (a) Tool (unit: mm), (b) FSW machine, (c) Dimension of the specimen for tension test (unit: mm)

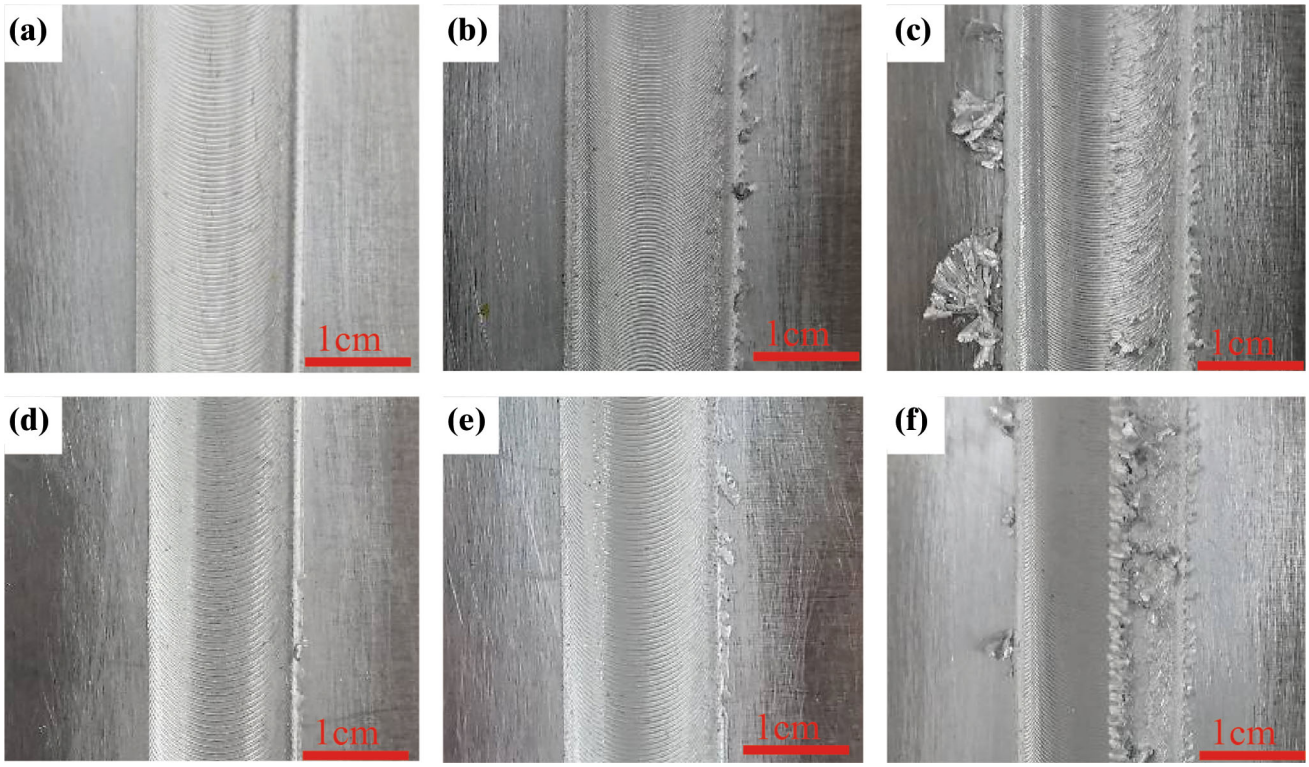

Fig. 2 Surface appearances of joints (a) 600-300, (b) 800-300, (c) 1000-300, (d) 600-400, (e) 800-400, (f) 1000-400, (unit: rpm-mm/min)

speeds of 600–1000 rpm and welding speeds of 300 and 400 mm/min. Assuming an ideal condition where the total work is converted into heat, the average heat input per unit time is obtained using an empirical equation (Ref 19).

$$Q = \frac{4\pi^2 \cdot \mu \cdot P \cdot \omega \cdot R^3}{3V} \quad \text{(Eq 1)}$$

where Q is the amount of heat generated, μ is the friction coefficient, P is the pressure, R is the shoulder radius, and ω and V are the tool rotation rate and welding speed, respectively. According to Eq. 1, the order of amount of heat input during welding is: $Q_{600\text{-}400} < Q_{600\text{-}300} < Q_{800\text{-}400} < Q_{800\text{-}300} < Q_{1000\text{-}400} < Q_{1000\text{-}300}$. The welding parameters are listed in Table 3. Six experiments were conducted to analyze the microstructure and mechanical properties.

After welding, microstructural studies were performed using a metallurgical microscope. The specimens were cut along the weld cross section, and then prepared by wet-grinding with water using different grades of emery paper, followed by polishing with diamond paste. The surfaces of the specimens were etched using Keller's solution (HNO_3: 5 mL, HCl: 3 mL, HF: 2 mL, H_2O: 190 mL). Microstructural examination of butt-welded joints was carried out via SEM and EDS.

The tensile tests were performed using a universal testing machine. The testing specimens were cut to the shape shown in Fig. 1(c) using wire cut electrical discharge machining (WEDM). Three specimens were obtained from each welded joint, and the average of the three specimens was taken as the test result. The fracture morphology was observed via SEM. Microhardness measurements were taken from the polished cross sections of the welds using a Vickers indenter with a load of 200 gf for 15 s.

3. Results and Discussions

3.1 Surface Morphology

The surface morphologies of the AA2024 and AA7075 FSW joints are shown in Fig. 2. The advancing side (AS) and retreating side (RS) are on the right and left of the photographs, respectively. There are no defects or cracks evident on the surfaces of any of the specimens. This indicates that FSW successfully connected the two different BMs when a suitable speed and feed rate were used. The interface features depend on the total heat input and temperature during welding (Ref 19). The welds in Fig. 2(a), (d), and (e) are smooth, whereas those in Fig. 2(b), (c), and (f) are rough. Arbegast (Ref 20) used the equation of maximum temperature of FSW (Eq. 2) to demonstrate the effects of the rotational and welding speeds.

$$\frac{T}{T_m} = K\left(\frac{\omega^2}{V \times 10^4}\right)^{\alpha} \quad \text{(Eq 2)}$$

where T is the FSW temperature (°C); T_m is the melting temperature of the sheet material (°C); $0.04 < \alpha < 0.06$ and $0.65 < K < 0.75$ are two defined constants; and ω and V are the tool rotational and welding speeds, respectively. Based on Eq. 2, the FSW temperature was related to the ω^2/V ratio. According to Eq. 2, the temperatures corresponding to Fig. 2(b), (c), and (f) are higher than those for Fig. 2(a), (d), and (e). Because of the increase in heat input, abnormal sticking of the pasty aluminum, and shearing under the shoulder can occur, making the surface of the weld less bright, and resulting in burrs and peeling (Ref 21).

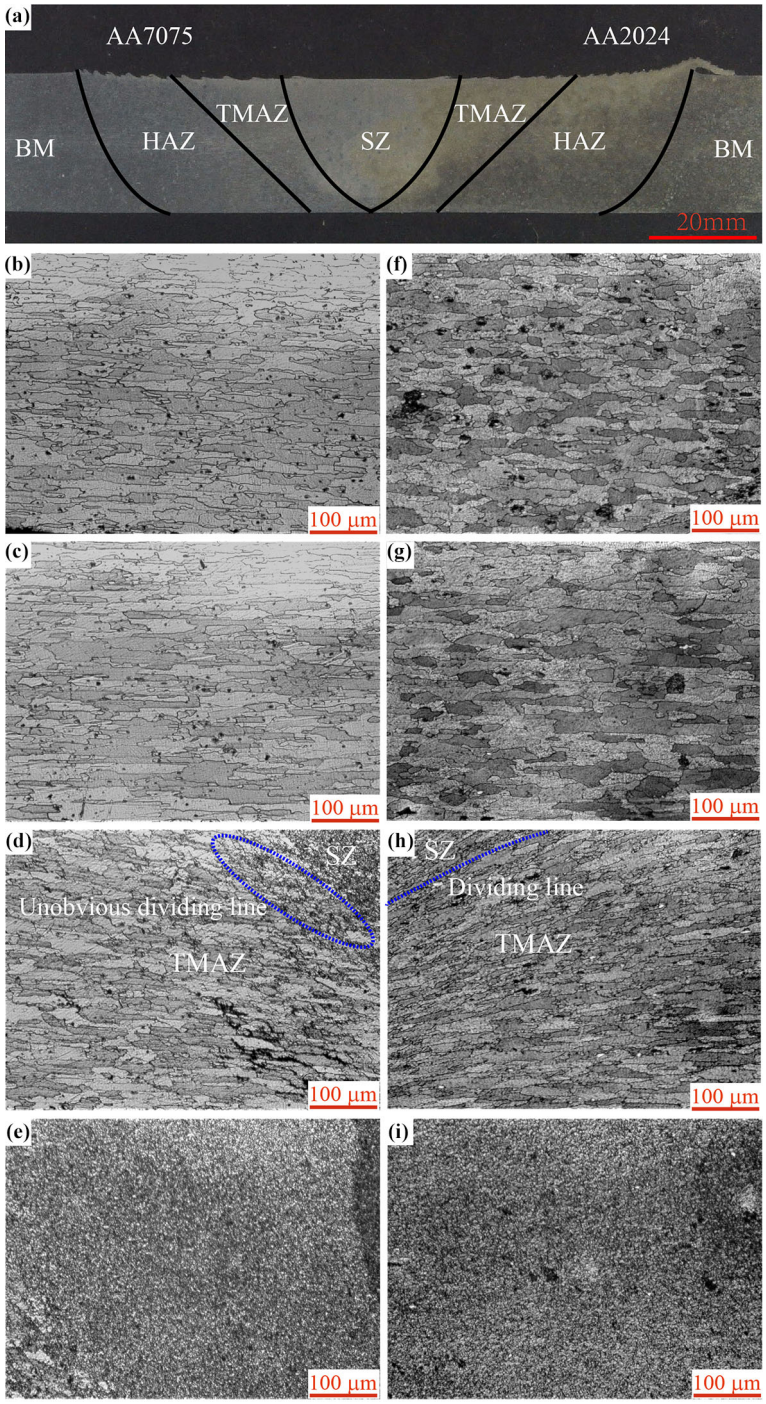

Fig. 3 Macro-image and microstructures of specimen 5: (a) macrostructure, (b–e) 7075 on RS, (f–i) 2024 on AS, (b, f) BM, (c, g) HAZ, (d, h) TMAZ and (e, i) SZ

3.2 Microstructural Observations

The stirring of the FSW tool causes a complex material to flow in the SZ. Figure 3(a) shows that AS (AA2024 BM) flows to RS (AA7075 BM). AA2024 accounts for most of the material in the SZ. The microstructure of the mixed interface of the two materials is relatively complex; the cross section of the joint is divided into four areas: SZ, TMAZ, HAZ, and BM. According to the results presented in Fig. 3(e) and (i), the SZ experienced high temperature and plastic deformation, so dynamic recrystallization occurred, and equiaxed and very fine grain structures could be observed. The material in the TMAZ was severely deformed, and had thin, twisted grains owing to deformation and high extrusion. Moreover, as shown in Fig. 3(d) and (h), sharper demarcation between the weld nugget and TMAZ was observed on the AS, and a more gradual transition from the weld nugget to the TMAZ was observed on the RS. Grains were observed on the AS oblique upward at 45°, but not on the RS. This is because of the plastic deformation in FSW. The linear velocity of the material at the RS is equal to the difference between the rotational speed and feed rate, and

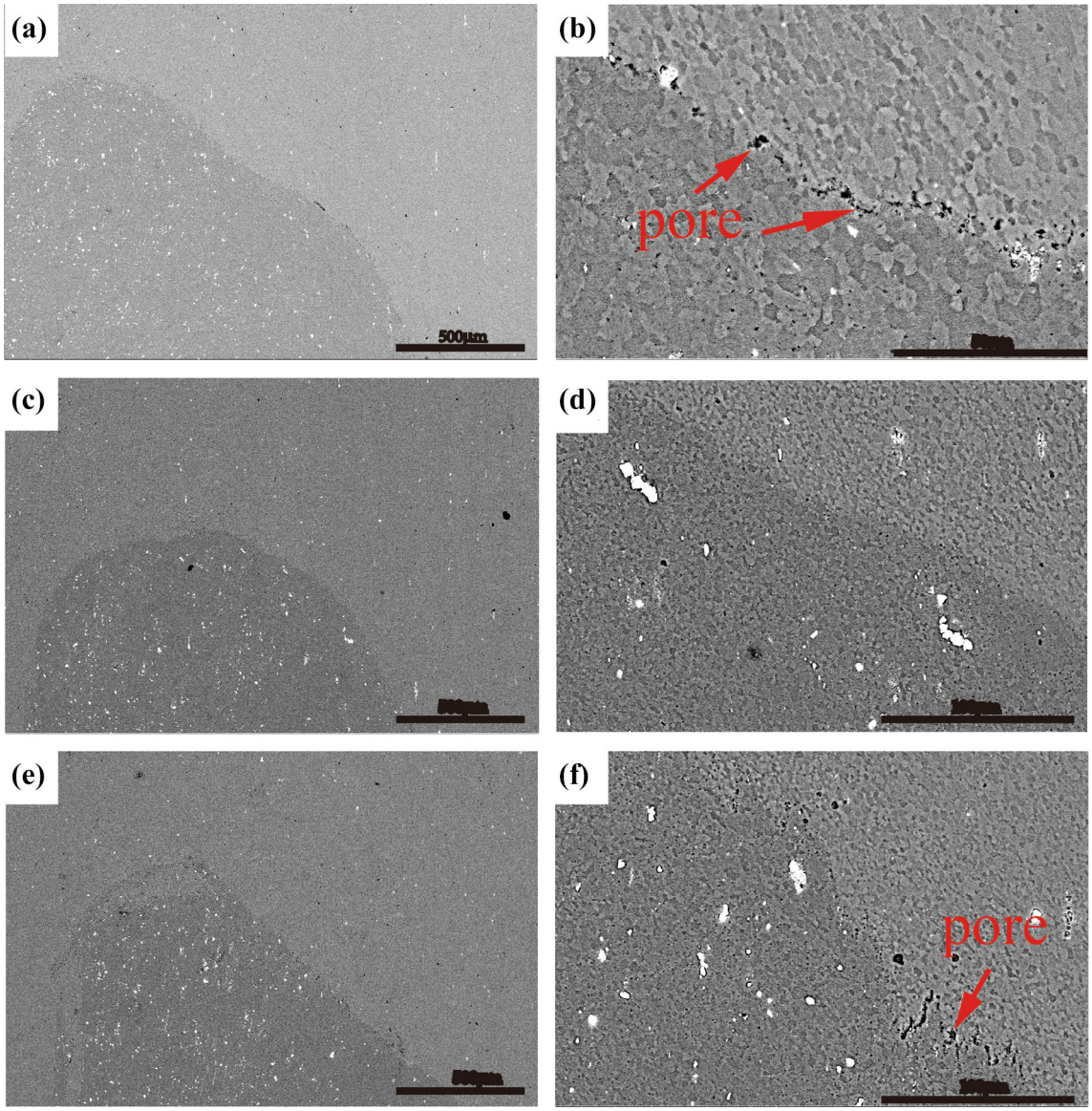

Fig. 4 SEM images of the SZ in the as-welded joints, (a, b) 1000 rpm-300 mm/min, (c, d) 800 rpm-400 mm/min, (e, f) 1000rpm-400 mm/min

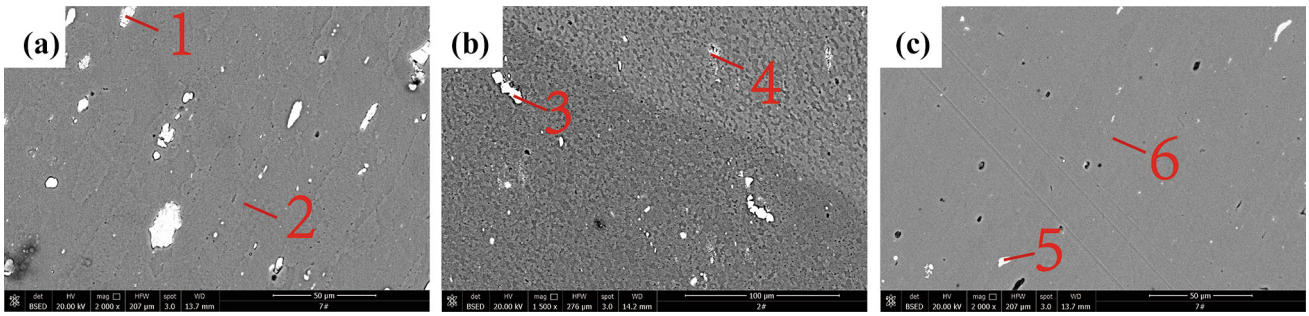

Fig. 5 SEM enlargement of (a) 2024 aluminum alloy BM, (b) SZ at 800 rpm-400 mm/min, (c) 7075 aluminum alloy BM

the linear velocity of the material at the RS is significantly lower than that at the AS. Therefore, the boundary on the RS is not as clear as that on the AS. However, the HAZ is only affected by the heat input; the grains are similar to those of the BM, but larger. Figure 3 shows that the grains of the BM AA2024 and AA7075 are oblong shaped. The quantities of

second-phase particles in the BM and HAZ are significantly more than in the SZ and TMAZ, because the SZ and TMAZ have experienced the influence of high thermal input during the welding process, which can dissolve the precipitates.

Figure 4 shows the SEM images of the SZ of the various welded joints. Figure 4(a), (c), and (e) shows that precipitates are distributed within the joint. Moreover, the precipitate distribution on the 2024 side is significantly denser than that on the 7075 side. Figure 4(b), (d), and (f) shows higher-magnification SEM images. Clear pores can be observed along the joint surfaces in Fig. 4(b) and (f), and the pores in Fig. 4 (b) are more significant than those in Fig. 4(f). These pores are a result of the high heat input and abnormal agitation of the material at high rotational speeds. Furthermore, owing to the high heat input, the cooling rate is faster, which can cause hole defects.

The SEM, EDS, and XRD analyses of the joints are shown in Fig. 5, Table 4, and Fig. 6, respectively. More Al_2Cu, AlCuMg, Al_2CuMg, and Cu_2FeAl_7 precipitates could be observed at the 2024 aluminum alloy side, whereas Cu_2FeAl_7 and $MgZn_2$ precipitates could be observed at the 7075 aluminum alloy side, which is consistent with the results of (Ref 22). Therefore, more precipitates form on the AA2024 side than on the AA7075 side, as shown in Fig. 4. There were AA2024 is richer in copper, while AA7075 contains more zinc.

Table 4 EDS scan element distributions at the points shown in Fig. 5 Atomic percent (%)

Spectrum	Mg	Al	Fe	Cu	Zn
1	–	56.03	5.11	31.84	–
2	2.23	95.77	–	1.76	–
3	–	65.05	–	33.27	–
4	3.52	89.69	–	1.71	5.08
5	0.84	75.27	16.64	5.77	1.19
6	1.94	95.79	0.01	0.59	1.58

Evidently, more precipitate phases containing copper were produced in the AS, whereas those containing zinc were produced in the RS. This is mainly determined by the corresponding BMs in the AS and RS, because of the high temperature and small plastic deformation during FSW. When there is less Fe, it could dissolve in the aluminum matrix; when there is more Fe, Cu_2FeAl_7 could be formed (Ref 23). Cu_2FeAl_7 is formed at high temperatures (and is also known as the β (Cu-Fe) or N phase), and more Cu_2FeAl_7 is formed on the AA7075 side. Particle analyses at point 4 show that these particles can be determined to be $S(Al_2CuMg)$. In addition, the particles in the SZ have a composition close to that of $MgZn_2$. As previously reported (Ref 24), there are two different types of precipitates in welded joints: $S(Al_2CuMg)$ and η ($MgZn_2$). Because of the high heat input, most of the precipitates (Cu_2FeAl_7 and $MgZn_2$) are dissolved in the SZ. Moreover, this is why there is more precipitation on the 2024 side than on the 7075 side.

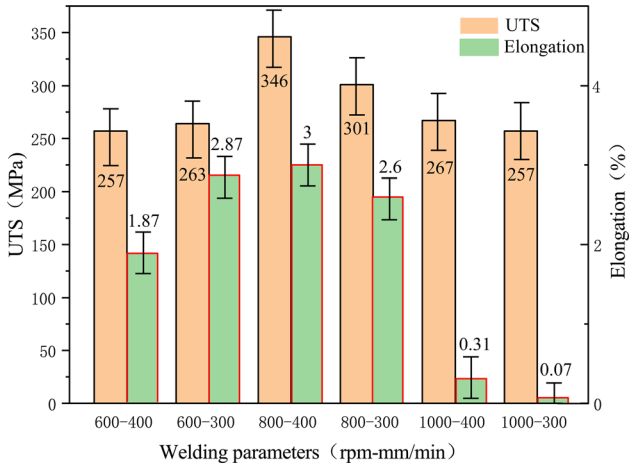

Fig. 7 The tensile properties of welded specimens

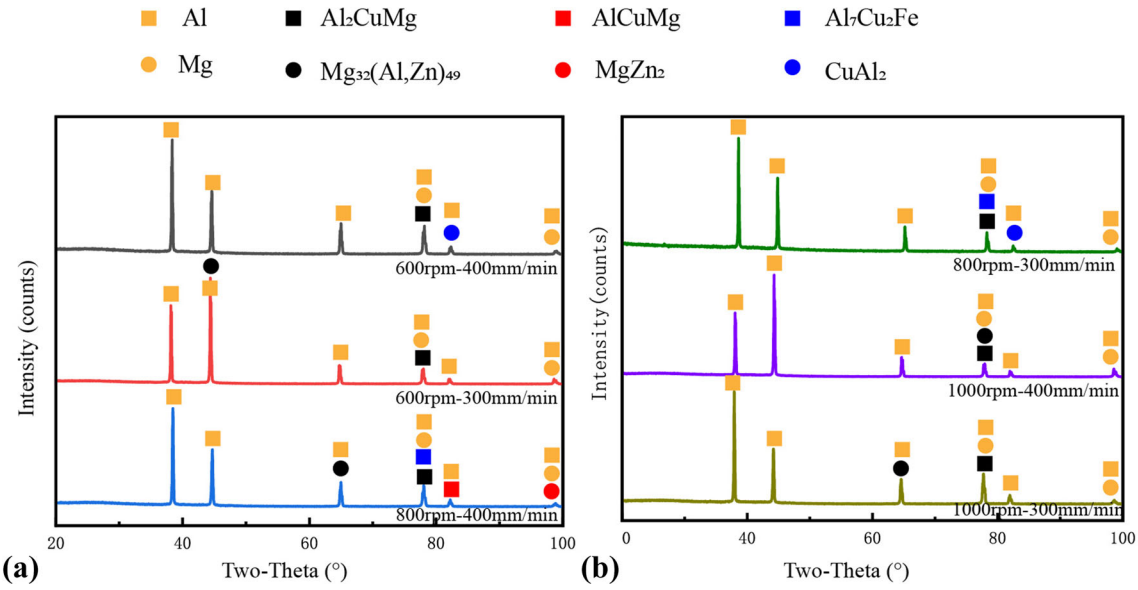

Fig. 6 XRD patterns of the joints

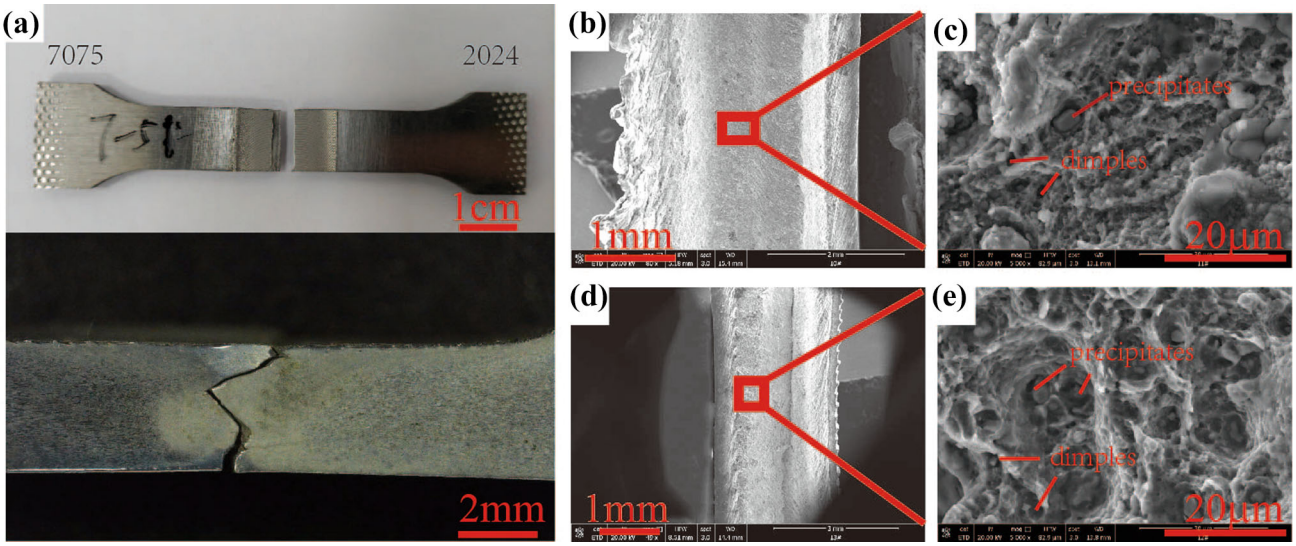

Fig. 8 (a) Tensile test fracture position of the sample at 800 rpm and 400 mm/min feed speed. SEM images at different magnifications of the fracture surfaces of tensile tests at (b, c) 1000 rpm and 300 mm/min; (d, e) 800 rpm and 400 mm/min

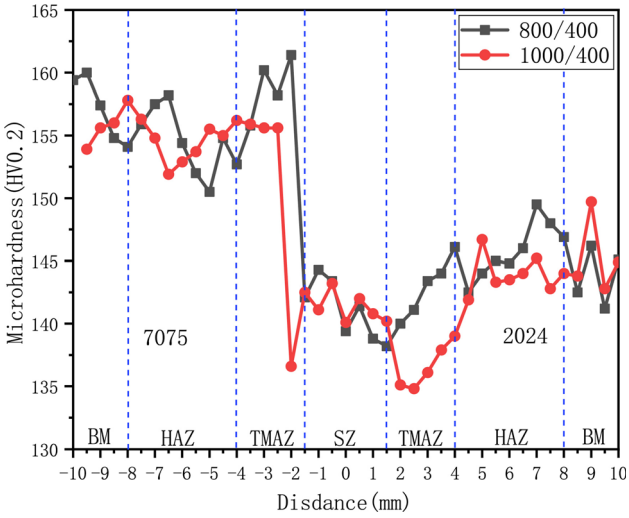

Fig. 9 Microhardness distribution of dissimilar FSW cross sections

3.3 Mechanical Characterization

To analyze the effect of the heat input on the tensile strength, the welded joints were subjected to tensile tests, and the fracture parameters—ultimate tensile strength (UTS) and elongation to break—were compared. The UTS values depend on the welding conditions, as shown in Fig. 7. The temperatures obtained under different welding parameters were calculated using Eq. 2, and were in the following order: $T_{600\text{-}400} < T_{600\text{-}300} < T_{800\text{-}400} < T_{800\text{-}300} < T_{1000\text{-}400} < T_{1000\text{-}300}$. When the welding parameter was 800 rpm–400 mm/min, the UTS of the joint was the highest (346 MPa), and the elongation was 3%. The minimum UTS of value obtained was 257 MPa, when the welding parameters were 600 rpm-400 mm/min and 1000 rpm–300 mm/min. This is because the 800 rpm-400 mm/min combination has a suitable heat input, which leads to enhanced precipitation in the SZ, resulting in a considerable amount of Al_2CuMg, $MgZn_2$, and other precipitates which improve tensile strength. A significantly higher or lower temperature results in lower tensile strength and elongation. This is because the heat input is too low to deform the material completely, and the fluidity of the material from the two BMs is poor during welding. In addition, increasing the temperature excessively causes a higher heat input. This could cause microstructural changes, such as precipitate dissolution, the grains becoming coarsened or thicker, and fewer grain boundaries (Ref 25). In addition, when the heat input is higher during welding, the cooling rate is faster, which could form hole defects on the welding interface and significantly affect the quality of the joint.

Figure 8(a) shows the fracture position of the tensile test specimen that was welded at a rotational speed of 800 rpm and a feed rate of 400 mm/min. The fracture locations of all samples were in the SZ, and no significant necking was observed. From the cross section of the fracture, it can be observed that fracture occurred at the bonding surface at the bottom of the weld, whereas the upper part of the weld was not on the bonding surface. This was also confirmed by the fracture scan shown in Fig. 8(b). The fracture location was similar to that reported in (Ref 26). During welding, owing to the difference in the heat gradient between the upper and lower parts of the weld, and the lower part being close to the bottom plate, there is insufficient heat input to the lower part of the weld. Stress concentration occurs at the bottom of the weld, and this could be the reason for the fracture being located in the SZ.

Fracture surface images of selected tensile specimens are shown in Fig. 8(b)–(e). All the fracture patterns are similar, as shown in the enlarged view. All fracture locations have dimples, which are associated with ductile fracture. The dimples on the sample welded with parameters of 800 rpm-400 mm/min are smaller and denser than on the sample welded with parameters of 1000 rpm-300 mm/min. The dimples are caused by the nucleation, growth, and coalescence of voids. These voids are formed because of the inhomogeneous rates of deformation in the material under the applied load (Ref 27).

The hardness was measured at 0.5 mm spacing across the welds, and two representative examples are shown in Fig. 9. According to Fig. 9, the hardness of AA7075 is higher than that of AA2024. Their values were approximately 161 and 143 HV, respectively. The microhardness chart of the joint shows that

the low-hardness areas of the joint are in the HAZ on the AA7075 side and at the interface between the SZ and TMAZ. Minimum hardness occurred at the junction of the SZ and TMAZ. This could be because the heat input is significantly higher, such that the hardening precipitates dissolve. The low hardness of the HAZ on the AA7075 side is attributed to the coarsening of the crystal grains and precipitates. This is consistent with the results of previous studies (Ref 28, 29). However, the hardness of SZ is slightly higher because of the fine equiaxed recrystallized grains in the SZ. As shown in the figure, the SZ becomes wider as the rotation speed increases.

4. Conclusions

1. Al_2Cu, Al_2CuMg, AlCuMg, and Cu_2FeAl_7 particles were detected on the AA2024 side in the SZ, whereas Cu_2FeAl_7 and $MgZn_2$ particles were present on the AA7075 side.
2. The 800 rpm-400 mm/min sample experienced the optimum heat input, and had the best tensile performance; its UTS reached 346 MPa, and elongation was 3%. Reaching a significantly high or low temperature during welding results decreases tensile strength and elongation.
3. The TMAZ exhibited the lowest hardness values in the joints. The thermal cycle generated via FSW leads to the coarsening of crystal grains and precipitated phases.
4. Because the thermal gradient is extremely large, the heat input at the bottom of the weld is insufficient; thus, the fracture position is in the SZ. Dimples were observed on the surface of the fracture, indicating that the fracture mode was ductile fracture.

Acknowledgment

This study was funded by Jiangxi Provincial Natural Science Foundation Project (20171BAB216033); Jiangxi Provincial Department of Education Science and Technology Research Project (GJJ170501); The cultivation project of the State key Laboratory of Green Development and High-value Utilization of Ionic Rare Earth Resources in Jiangxi Province (20194AFD44003); Jiangxi Provincial Natural Science Foundation Project (20171BAB206030); Ganzhou Science and Technology Plan Project Science and Technology Innovation Talent Program; Ganzhou Science and Technology Plan Project; Jiangxi University of Science and Technology PhD Foundation Funded Project (JXXJBS16001). We thank Kate Nairn, PhD, from Liwen Bianji (Edanz) (www.liwenbianji.cn/), for editing the English text of a draft of this manuscript. We would like to thank Editage (www.editage.cn) for English language editing.

Author's contribution

Shun Xiao: Conceptualization, Methodology, Validation, Formal analysis, Investigation, Writing-Original Draft, Writing-Revive & Editing. Yongfang Deng: Writing-Revive & Editing, Resources, Funding acquisition. Jingcheng Zeng: Conceptualization, Methodology. Weichao Zhang: Investigation. Lirong Huang: Writing-Revive, Funding acquisition. All authors agree to participate in the completion of the manuscript and the publication of the manuscript.

Declarations

Ethical Approval

The submitted work is original and has not been published elsewhere. The manuscript was not been submitted to more than one journal for simultaneous consideration.

Conflict of interests

The authors declare that they have no known competing financial interests or personal relationships that could have appeared to influence the work reported in this paper.

References

1. M.L. de Bonfils-Lahovary, L. Laffont, C. Blanc, Characterization of intergranular corrosion defects in a 2024-T351 aluminum alloy[J], *Corros Sci*, 2017, **119**, p 60–67
2. S. Li, H. Dong, L. Shi et al., Corrosion behavior and mechanical properties of Al-Zn-Mg aluminum alloy weld, *Corros Sci*, 2017, **123**, p 243–255
3. J.Q. Su, T.W. Nelson, R. Mishra et al., Microstructural investigation of friction stir welded 7050–T651 aluminium, *Acta Mater.*, 2003, **51**(3), p 713–729
4. C. Genevois, A. Deschamps, A. Denquin et al., Quantitative investigation of precipitation and mechanical behaviour for AA2024 friction stir welds, *Acta Mater*, 2005, **53**(8), p 2447–2458
5. A. Fattah-Alhosseini, M. Naseri, D. Gholami et al., Microstructure and corrosion characterization of the nugget region in dissimilar friction-stir-welded AA5083 and AA1050, *J Mater Sci*, 2019, **54**(1), p 777–790
6. R. Manikandan and G. Elatharasan, Effect of process parameters on microstructural and mechanical properties of friction stir welded dissimilar aluminium alloys AA 6061 and AA 7075, *Int. J. Rapid Manuf.*, 2020, **9**(1), p 1–15
7. P. Liu, S. Sun, S. Xu et al., Microstructure and properties in the weld surface of friction stir welded 7050–T7451 aluminium alloys by laser shock peening, *Vacuum*, 2018, **152**, p 25–29
8. V. Balasubramanian and A.K. Lakshminarayanan, The mechanical properties of the GMAW, GTAW and FSW joints of the RDE-40 aluminium alloy, *Int. J. Microstruct. Mater. Prop.*, 2008, **3**(4–5), p 837–853
9. Z.Y. Ma, A.H. Feng, D.L. Chen et al., Recent Advances in Friction stir welding/processing of aluminum alloys: microstructural evolution and mechanical properties, *Crit. Rev. Solid State Mater. Sci.*, 2018, **43**(4), p 269–333
10. L. Dubourg, A. Merati and M. Jahazi, Process optimisation and mechanical properties of friction stir lap welds of 7075–T6 stringers on 2024–T3 skin, *Mater. Des.*, 2010, **31**(7), p 3324–3330
11. I. Radisavljevic, A. Zivkovic, N. Radovic et al., Influence of FSW parameters on formation quality and mechanical properties of Al 2024–T351 butt welded joints, *Trans Nonferrous Metals Soc China (English Edition)*, 2013, **23**(12), p 3525–3539
12. S. Entesari, A. Abdollah-Zadeh, N. Habibi et al., Experimental and numerical investigations into the failure mechanisms of friction stir welded AA7075-T6 thin sheets, *J Manuf Process*, 2017, **29**(Oct), p 74–84
13. T.S. Rao, G.M. Reddy and S. Rao, Microstructure and mechanical properties of friction stir welded AA7075–T651 aluminum alloy thick plates, *Trans Nonferrous Metals Soc China*, 2015, **25**(6), p 1770–1778
14. C.G. Rhodes, M.W. Mahoney, W.H. Bingel et al., Effects of friction stir welding on microstructure of 7075 aluminum, *Scripta Mater*, 1997, **36**(1), p 69–75

15. C.G. Zhang, G.J. Huang, Y. Cao et al., Microstructure evolution of thermo-mechanically affected zone in dissimilar AA2024/7075 joint produced by friction stir welding, *Vacuum*, 2020, **179**, p 109515
16. M.M. Moradi, J. Aval, R. Jamaati et al., Microstructure and texture evolution of friction stir welded dissimilar aluminum alloys: AA2024 and AA6061, *J. Manuf. Process.*, 2018, **32**, p 1–10
17. H.K. Rafi, G.D.J. Ram, G. Phanikumar et al., Microstructure and tensile properties of friction welded aluminum alloy AA7075-T6, *Mater. Des.*, 2010, **31**(5), p 2375–2380
18. F.J. Liu, L. Fu and H.Y. Chen, Microstructure evolution and fracture behaviour of friction stir welded 6061–T6 thin plate joints under high rotational speed, *Sci Technol Weld Joi*, 2017, **23**(4), p 1–11
19. M. Ghosh, K. Kumar and R.S. Mishra, Friction stir lap welded advanced high strength steels: microstructure and mechanical properties, *Mat Sci Eng A-Struct*, 2011, **528**(28), p 8111–8119
20. D. Harris and A.F. Norman, Effect of welding heat input and post-welded heat treatment on hardness of stir zone for friction stir-welded 2024–T3 aluminum alloy, *Trans Nonferrous Metals Soc China*, 2015, **25**(8), p 2524–2532
21. H. Bisadi, A. Tavakoli, M.T. Sangsaraki et al., The influences of rotational and welding speeds on microstructures and mechanical properties of friction stir welded Al5083 and commercially pure copper sheets lap joints, *Mater Design*, 2013, **43**(JAN), p 80–88
22. H. Aydin, A. Bayram and I. Durgun, The effect of post-weld heat treatment on the mechanical properties of 2024–T4 friction stir-welded joints, *Mater Design*, 2010, **31**(5), p 2568–2577
23. C.H. Zhang, G.G. Huang, Y. Gao et al., Microstructure evolution of thermo-mechanically affected zone in dissimilar AA2024/7075 joint produced by friction stir welding, *Vacuum*, 2020, **179**, p 109515
24. N. Birbilis, M.K. Cavanaugh and R.G. Buchheit, Electrochemical behavior and localized corrosion associated with Al7Cu2Fe particles in aluminum alloy 7075–T651, *Corrosion Sci*, 2006, **48**(12), p 4202–4215
25. M. Navaser and M. Atapour, Effect of friction stir processing on pitting corrosion and intergranular attack of 7075 aluminum alloy, *J Mater Sci Technol*, 2017, **033**(002), p 155–165
26. O.P. Abolusoro, E.T. Akinlabi and S.V. Kailas, Tool rotational speed impact on temperature variations, mechanical properties and microstructure of friction stir welding of dissimilar high-strength aluminium alloys, *J Braz Soc Mech Sci*, 2020, **42**, p 176
27. M. Ghosh, K. Kumar and R.S. Mishra, Friction stir lap welded advanced high strength steels: microstructure and mechanical properties, *Mater. Sci. Eng., A*, 2011, **528**(28), p 8111–8119
28. S. Malopheyev, I. Vysotskiy et al., Optimization of processing-microstructure-properties relationship in friction-stir welded 6061–T6 aluminum alloy, *Mater. Sci. Eng., A*, 2016, **662**, p 136–143
29. L.E. Murr, G. Liu and J.C. Mcclure, A TEM study of precipitation and related microstructures in friction-stir-welded 6061 aluminium, *J. Mater. Sci.*, 1998, **33**(5), p 1243–1251